Heteroatom-doped helical carbonaceous nanotubes with ultrafine SnO_2 nanoparticles as active anode for lithium-ion batteries

Nan Wu,[†a] Huijuan Yao,[†a] Wenchao Liu,[a] Wei Zhang,[a] Rui Cao,[a] Haoquan Zheng,*[ab] and Hang Zhang*[a]

[a] Key Laboratory of Applied Surface and Colloid Chemistry, Ministry of Education, School of Chemistry and Chemical Engineering, Shaanxi Normal University, Xi'an 710119, China.

[b] Shanghai Key Laboratory of High-resolution Electron Microscopy, ShanghaiTech University, Shanghai 201210, China.

[†]These authors contributed equally to this work.

*Corresponding author:

E-mail addresses: zhenghaoquan@snnu.edu.cn (H. Zheng); zhangteacher@snnu.edu.cn (H. Zhang)

Experiment section

1. Preparation of SnO_2@NPSC

Preparation of Sn@PPy Precursor: *N*-Stearyl-L-glutamic acid (C_{18}-L-Glu) was initially prepared according to the literature method.[1,2,3] Subsequently, 24.5 mg of C_{18}-L-Glu was dissolved in 12.9 mL of methanol to form the template structure. After stirring for 30 min, 0.166 mL of pyrrole and 60 mL of deionized (DI) water were added dropwise sequentially. At the same time, 1.2 mL of pre-cooled aqueous solution containing 548 mg of ammonium persulfate and 60 mg of anhydrous $SnCl_2$ was introduced. The polymerization process was continuous under vigorous stirring for an additional 30 min. The black solid was collected by vacuum filtration, thoroughly washed with DI water and ethanol, and dried at 60 °C for 12 h to yield the precursor.

Preparation of Sn@NC: The Sn@PPy was calcined at 700 °C for 2 h in a tube furnace under argon atmosphere with a programmed heating rate of 2 °C min^{-1} to yield Sn@NC.

Preparation of SnO_2@NC: 90 mg of Sn@NC powder was dispersed in 25 mL of nitric acid solution and stirred at room temperature for 20 min. The resulting product was collected by centrifugation, washed repeatedly with deionized water and ethanol, and dried under vacuum at 60 °C for 12 h to obtain SnO_2@NC.

Preparation of SnO_2@NPSC: 30 mg of SnO_2@NC, 76 mg of thiourea, and 53 mg of sodium hypophosphite monohydrate were added to 30 mL DI water under stirring for 30 min. The homogeneous mixture was transferred into a Teflon-lined autoclave and maintained at 120 °C for 3 h. After natural cooling to room temperature, the product was isolated by centrifugation, alternately washed with ethanol and DI water three times, and vacuum-dried at 60 °C to afford SnO_2@NPSC.

2. *Preparation of SnO_2/NPSC*

120 mg of PPy and 60 mg of $SnCl_2$ were dispersed in 20 mL of DI water. After 1 h of ultrasonic treatment followed by 3 h of standing, the mixture was rotary-evaporated and dried to obtain Sn/PPy. The subsequent treatment procedure was consistent with the preparation method of SnO_2@NPSC.

3. *Preparation of SnO_2@NSC and SnO_2@NPC*

The preparation method was identical to that of SnO_2@NPSC, except that the phosphorus source or sulfur source was omitted during the hydrothermal process, respectively.

4. ***Preparation of SnO_2 (SnO_2-Bulk and SnO_2-Tube)***

The Sn@PPy precursor was calcined in air at 700 °C for 2 h with a heating rate of 2 °C min^{-1} to obtain SnO_2-Bulk. The SnO_2@NPSC was calcined in air at 700 °C for 2 h with a heating rate of 2 °C min^{-1} to obtain SnO_2-Tube.

5. ***Materials and characterizations***

All reagents were of analytical grade and used as received without further purification. The microstructure and elemental distribution of the composites were characterized by field-emission scanning electron microscopy (FESEM, HITACHI SU8220) and transmission electron microscopy (TEM, FEI Tecnai G2 F20). Phase composition and crystal structure were analyzed using X-ray diffraction (XRD, Bruker D8 DISCOVER A25, Cu Kα radiation). The structural features of the carbon matrix were examined by Raman spectroscopy (HORIBA LabRAM Odyssey). The surface chemical states and bonding environment were investigated using Fourier-transform infrared spectroscopy (FTIR, Bruker Tensor II) and X-ray photoelectron spectroscopy (XPS, Kratos Axis UltraDLD). The thermogravimetric (TG) curve of the sample was determined using thermal analyzer (SETARAM Themys one). The physisorption was carried out to provide the information for the calculation of specific surface area and pore size distribution (Micromeritics ASAP 2020).

6. ***Electrochemical measurements***

The electrochemical performance was evaluated using CR2032 coin-type cells. To prepare the working electrode, the as-synthesized material, acetylene black, and polyvinylidene fluoride (PVDF) were mixed in a mass ratio of 7:2:1 in N-methyl-2-pyrrolidone (NMP) to form a homogeneous slurry. The slurry was coated uniformly onto copper foil and dried at 90 °C under vacuum for 12 h. The mass loading of the active material on each electrode was controlled at approximately 1.0 mg cm^{-2}. Lithium metal foil was used as both the counter and reference electrodes. The electrolyte consisted of 1.0 M $LiPF_6$ dissolved in a mixture of EMC, EC, and DMC (volume ratio 1:1:1). A Celgard 2400 membrane was employed as the separator. Galvanostatic cycling tests, rate capability assessments, and galvanostatic intermittent titration technique (GITT) measurements were carried out within a voltage window of 0.01–3.0 V using a CT-4008 multi-channel battery test system (Shenzhen NEWARE Co., Ltd., China). Cyclic voltammetry (CV) and electrochemical impedance spectroscopy (EIS) were performed on a CHI660e electrochemical workstation (Chenhua, Shanghai, China).

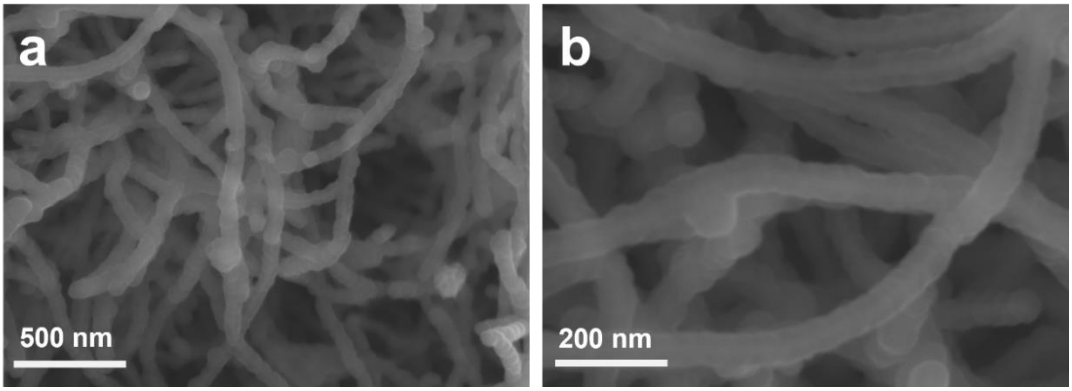

Fig. S1 SEM images of Sn@PPy.

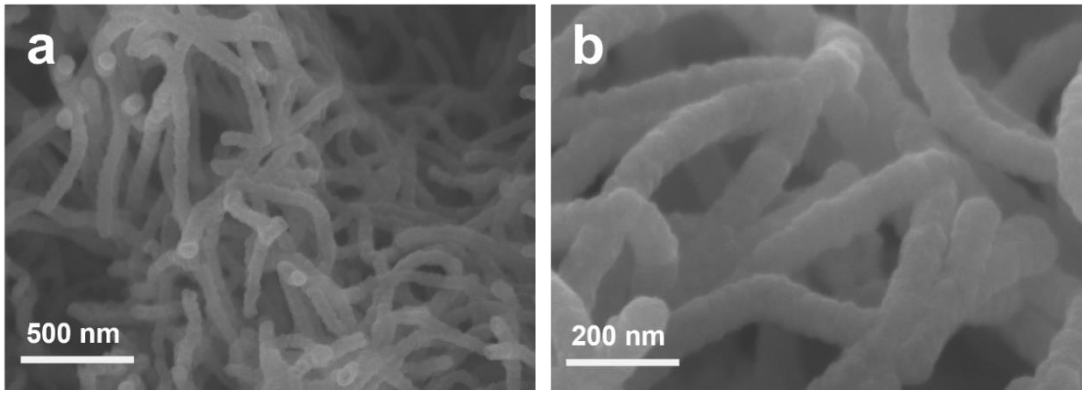

Fig. S2 SEM images of Sn@NC.

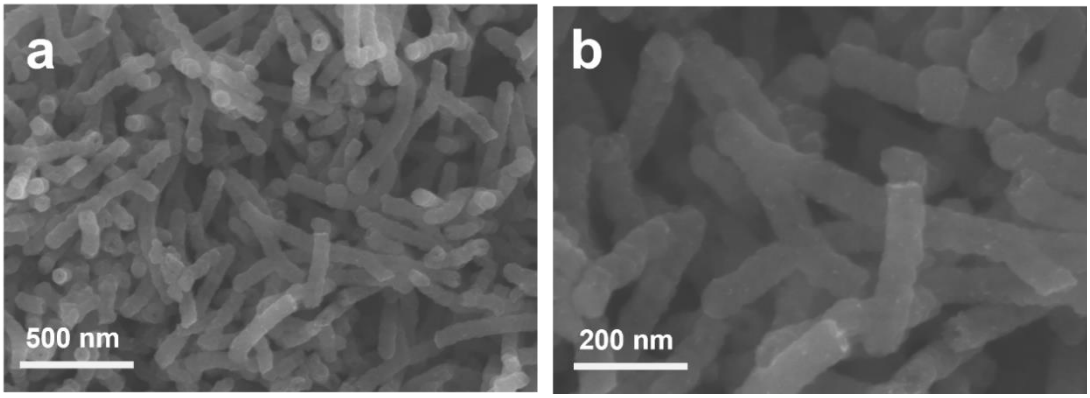

Fig. S3 SEM images of SnO_2@NC.

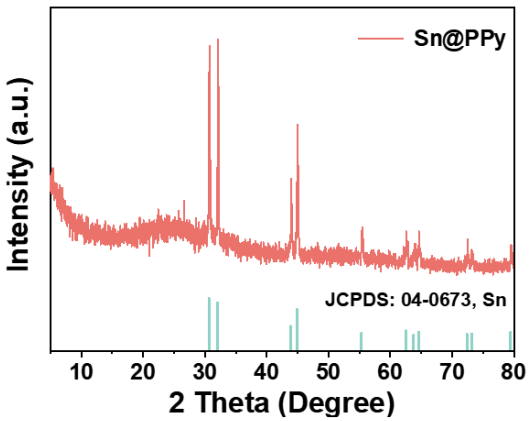

Fig. S4 XRD pattern of Sn@PPy.

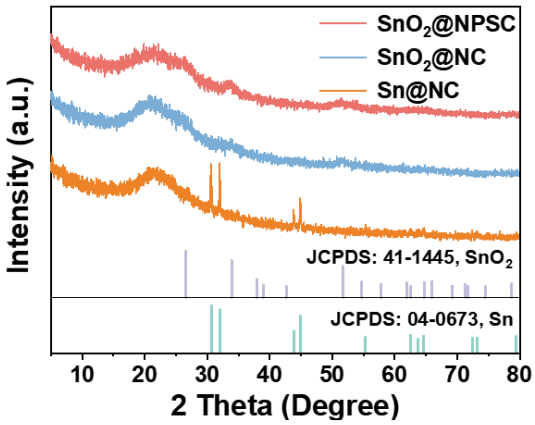

Fig. S5 XRD patterns of Sn@NC, SnO_2@NC, and SnO_2@NPSC.

The powder X-ray diffraction (PXRD) patterns of Sn@PPy and Sn@NC are shown in Fig. S4 and Fig. S5, respectively. The broad peak at about 25° indicates the conversion of polypyrrole precursor into carbon-based material. The peaks at 30.64°, 32.01°, 43.87°, 44.90°, and 55.33° correspond to the Sn (PDF #04-0673), which indicates that the Sn was successfully introduced into the structure. In contrast, the characteristic peaks of SnO_2@NC and SnO_2@NPSC located at 26.61°, 33.89°, and 51.78° are indexed to the (110), (101), and (211) crystal planes of SnO_2 (PDF #41-1445), respectively, confirming the complete oxidation of Sn.

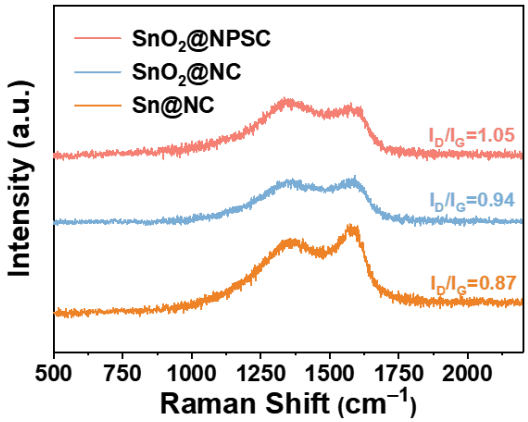

Fig. S6 Raman spectra of Sn@NC, SnO_2@NC, and SnO_2@NPSC.

The structural defects in the samples were analyzed using Raman spectroscopy (Fig. S6). Characteristic peaks were observed at 1347 cm^{-1} (D band) and 1576 cm^{-1} (G band), corresponding to the disordered amorphous carbon and the ordered graphitic carbon, respectively. The increased I_D/I_G value of SnO_2@NC (0.94) compared to Sn@NC (0.87) may be attributed to the introduction of oxygen-containing functional groups onto the carbon surface during nitric acid oxidation. The I_D/I_G value of SnO_2@NPSC (1.05) further increased, suggesting that P and S co-doping induce lattice distortion in the carbon framework and create additional structural defects, facilitating the lithium storage reaction.

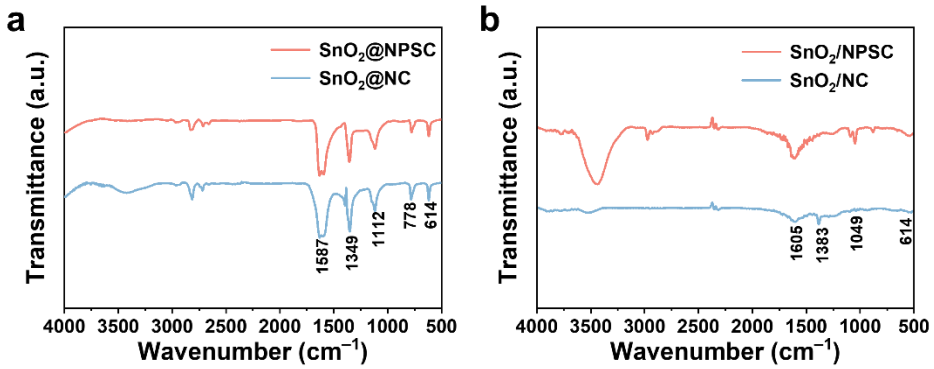

Fig. S7 (a) FT-IR spectra of SnO_2@NC and SnO_2@NPSC, (b) FT-IR spectra of SnO_2/NC and SnO_2/NPSC.

Fig. S7a presents the FT-IR analysis, which clearly tracks the structural evolution from SnO_2@NC to SnO_2@NPSC. The absorption bands at 1587 and 1349 cm^{-1} correspond to the carbon skeleton formed after calcination, while the sharp peak at 614 cm^{-1} confirms the formation of SnO_2. In the SnO_2@NPSC spectrum, the successful co-modification with P and S is evidenced by a slight shift of the Sn–O–Sn stretching vibration to lower wavenumbers, which can be attributed to electron redistribution resulting from the formation of P–O bonds. A similar trend is observed in Fig. S7b.

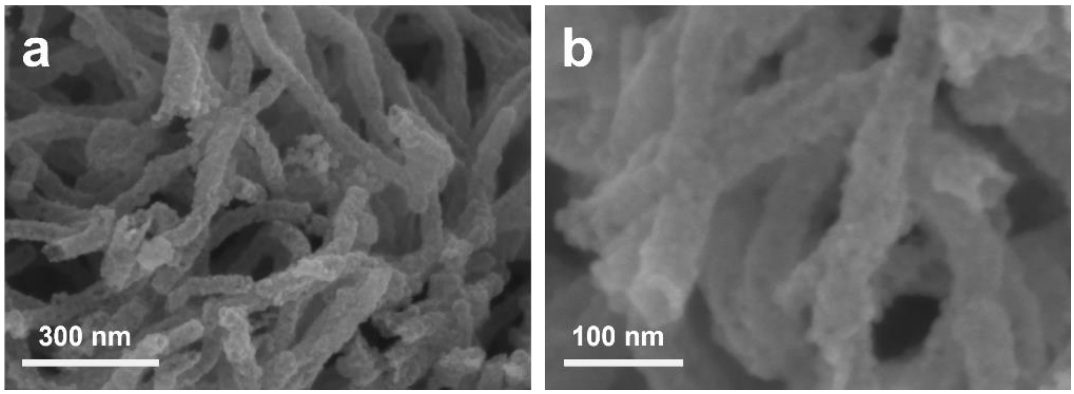

Fig. S8 SEM images of SnO_2-Tube.

SnO_2-Tube was used to further confirm the dispersion state of Sn-based species in SnO_2@NPSC, which was prepared by selectively removing carbon from SnO_2@NPSC through calcination in air. SEM results clearly show that the residual SnO_2 maintains the original carbon skeleton of tubular structure. This result clearly demonstrates that Sn-based species are homogeneously dispersed as ultrafine particles in SnO_2@NPSC, rather than existing as isolated or aggregated particles.

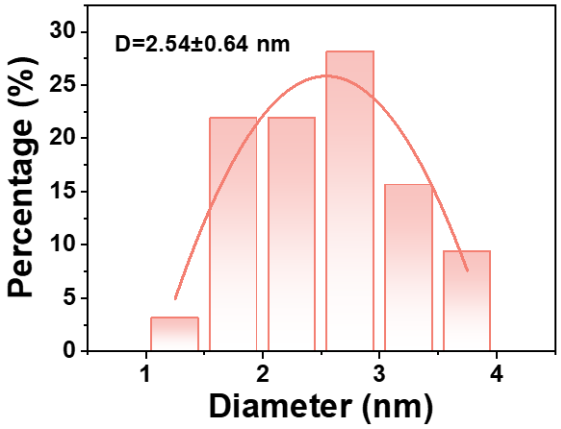

Fig. S9 Statistical histogram of particle size distribution for SnO_2@NPSC.

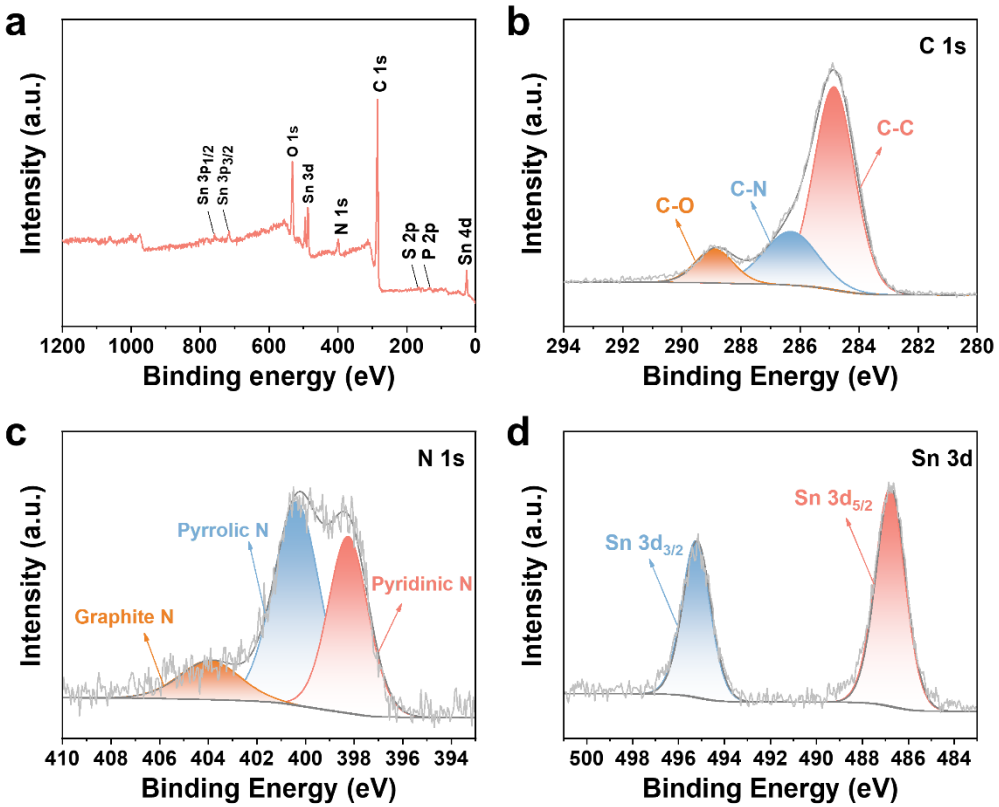

Fig. S10 (a) XPS full spectrum of SnO_2@NPSC. High-resolution XPS spectra of SnO_2@NPSC composite: C 1s (b), N 1s (c), and Sn 3d (d).

The survey spectrum (Fig. S10a) confirms that the composite is constituted of six elements, including Sn, O, N, C, S, and P, which is in good agreement with the TEM elemental mapping results. The C 1s (Fig. S10b) and N 1s (Fig. S10c) spectra verify the N-doped carbon skeleton with active nitrogen species (pyridinic/pyrrolic N) and conductive graphitic N. The characteristic Sn 3d doublet with a peak separation of 8.4 eV unambiguously identifies the Sn^{4+} oxidation state, confirming the successful and complete conversion of metallic Sn to SnO_2 during the oxidation treatment (Fig. S10d).[4]

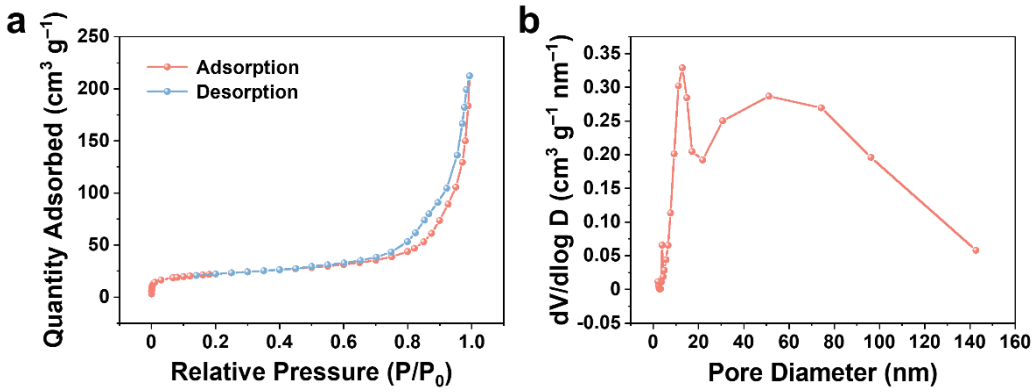

Fig. S11 Nitrogen adsorption-desorption isotherms (a) and pore size distribution (b) of SnO_2@NPSC.

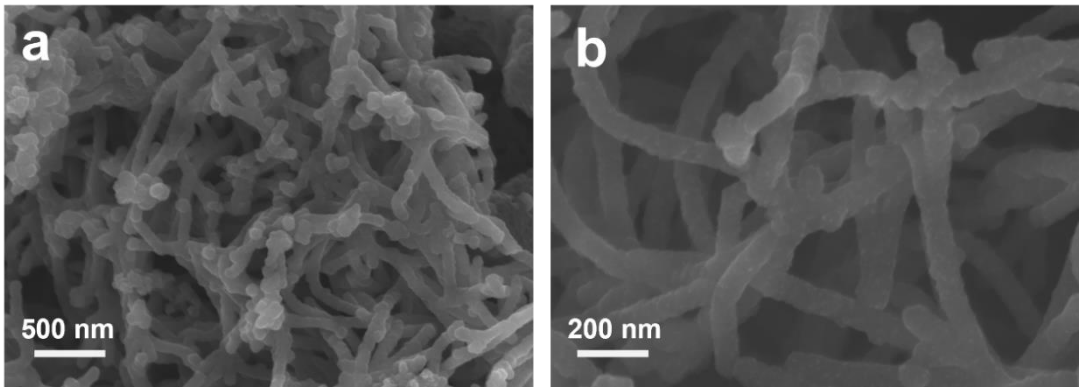

Fig. S12 SEM images of SnO_2/NPSC.

SEM images of SnO_2/NPSC and SnO_2-Bulk are presented in Fig. S12 and S13. Benefiting from the physical confinement and chemical bonding of the helical carbon nanotubes, the SnO_2 in the resulting SnO_2/NPSC composite maintains an ultrafine particle size and uniform dispersion (Fig. S12). Obviously, the SnO_2-Bulk in Fig. S13, which lacks this carbon skeleton, forms large, unstructured agglomerates.

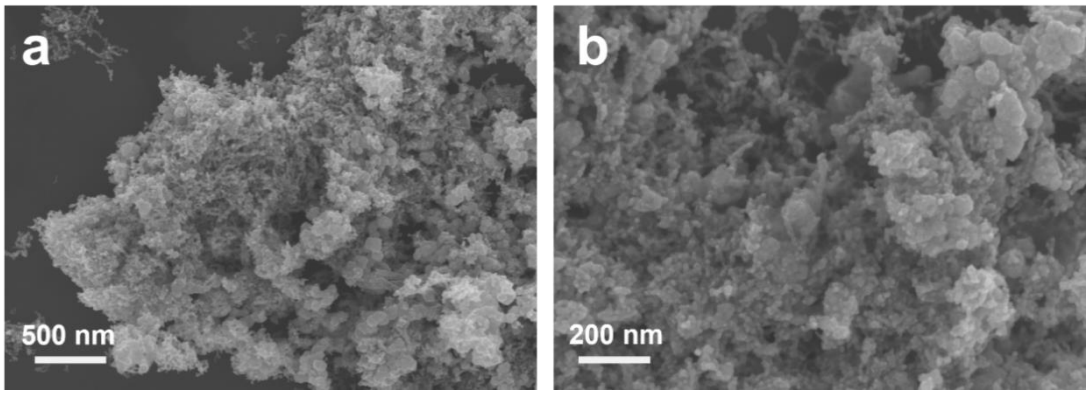

Fig. S13 SEM images of SnO_2-Bulk.

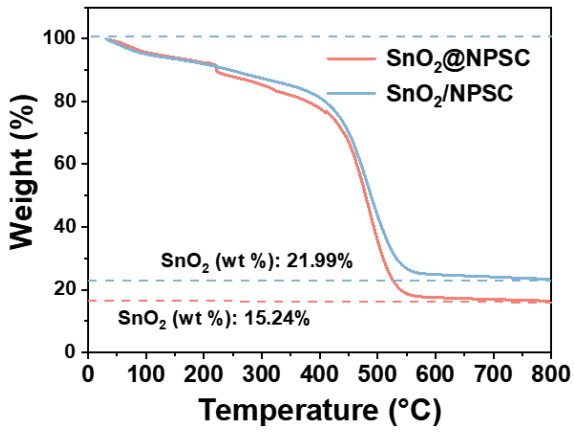

Fig. S14 Thermogravimetric analysis (TGA) of SnO_2@NPSC and SnO_2/NPSC composites.

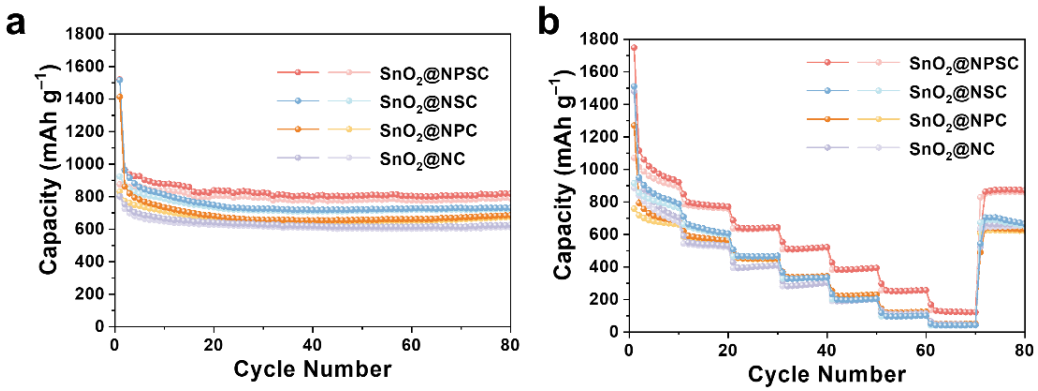

Fig. S15 Cycling performance at 0.1 A g^{-1} (a) and rate capability (b) of SnO_2@NPSC, SnO_2@NSC, SnO_2@NPC, and SnO_2@NC.

As shown in Fig. S15a, all control samples exhibit good cycling stability at a current density of 0.1 A g^{-1}. However, the SnO_2@NPSC electrode delivers the highest specific capacity and maintains this significant advantage throughout the entire cycling process, indicating that ternary co-doping possesses a distinct advantage in enhancing lithium storage capacity. Fig. S15b further presents the rate performance at various current densities. The SnO_2@NPSC electrode demonstrates superior capacity retention at all current densities.

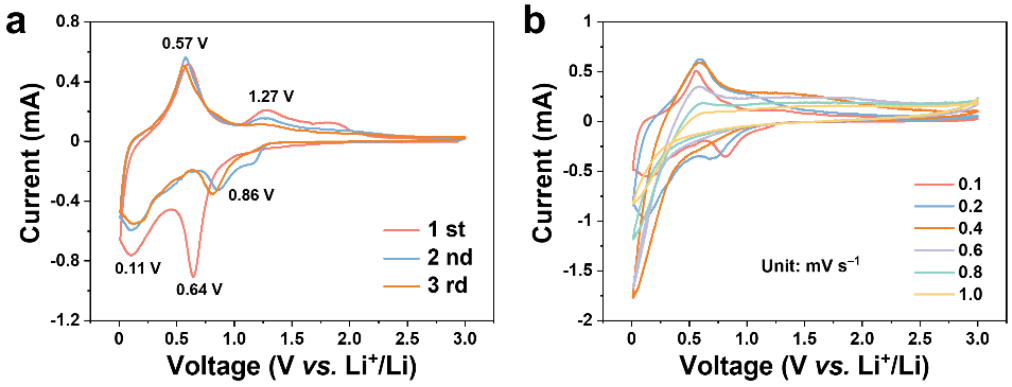

Fig. S16 CV curves for the first three revolutions at a scan rate of 0.1 mV s^{-1} (a) and CV curves at different scan rates (b) of SnO_2-Bulk.

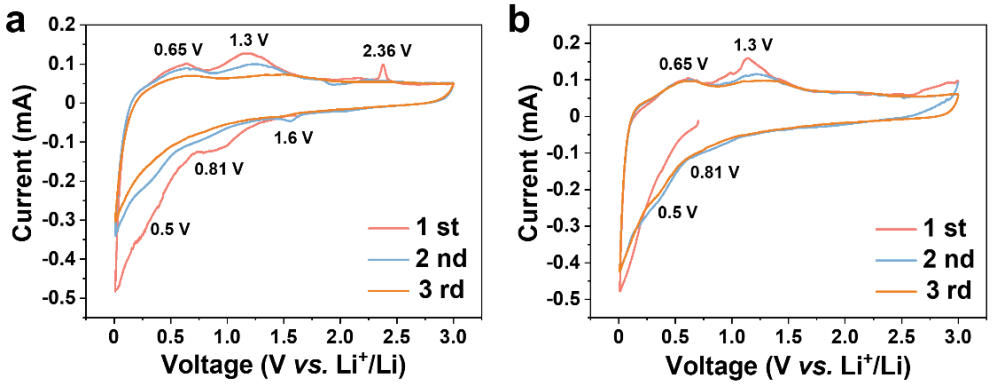

Fig. S17 CV curves of SnO_2@NSC (a) and SnO_2@NPC (b).

To gain a deeper understanding of the contributions from each doping element, the CV curves of the control samples were analyzed. Fig. S17a and S17b show the CV curves of SnO_2@NSC and SnO_2@NPC, respectively. Notably, the CV curve of SnO_2@NSC shows an oxidation peak at approximately 2.36 V that can be attributed to the partial irreversible loss of doped atoms from their reaction with solvated Li^+, whereas this peak is not observed in the CV curve of SnO_2@NPC. Apart from this, the positions of the other redox peaks are generally consistent with those of the SnO_2@NPSC electrode.

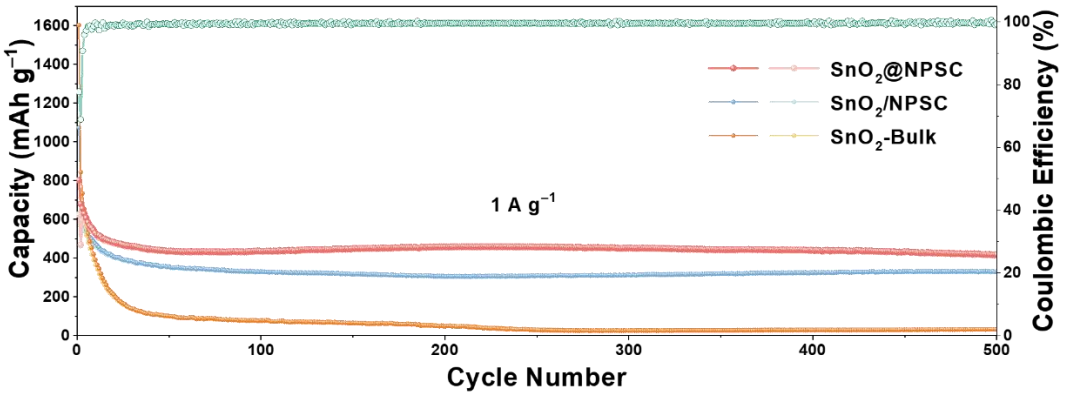

Fig. S18 Long-term cycling performance at 1 A g^{-1} of SnO_2@NPSC, SnO_2/NPSC, and SnO_2-Bulk.

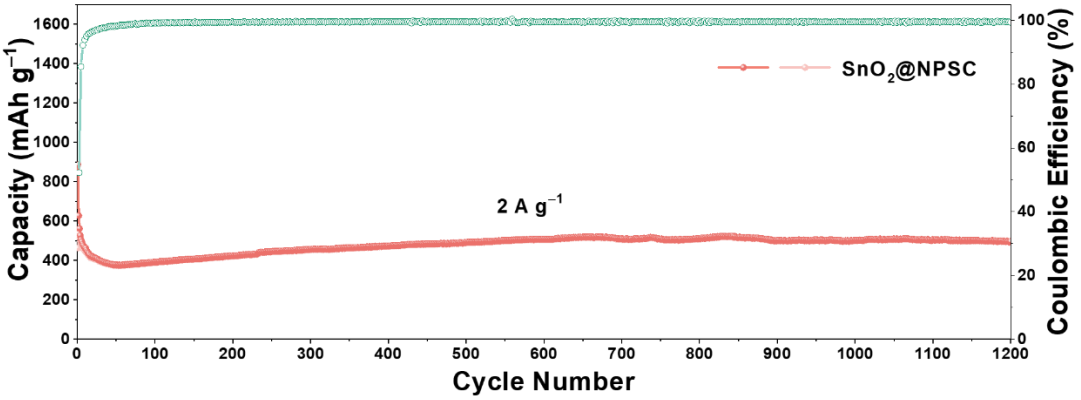

Fig. S19 Long-term cycling performance at 2 A g^{-1} of SnO_2@NPSC.

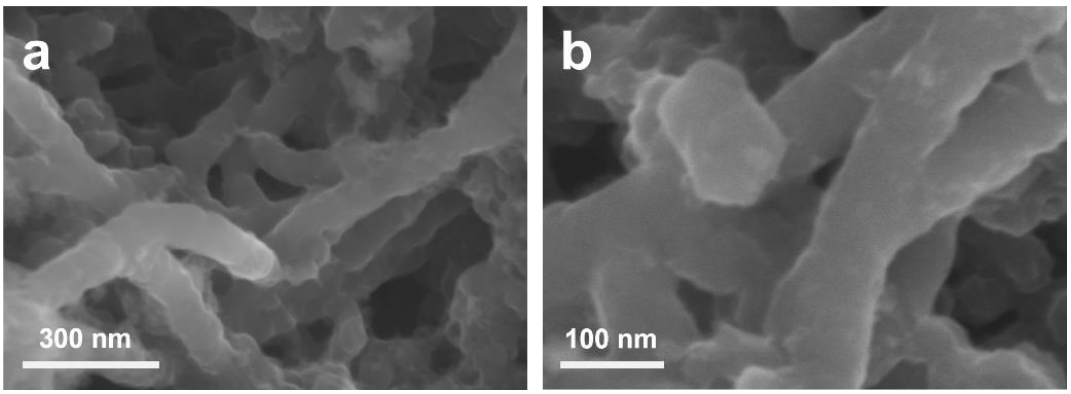

Fig. S20 SEM images of the SnO_2@NPSC electrode after cycling.

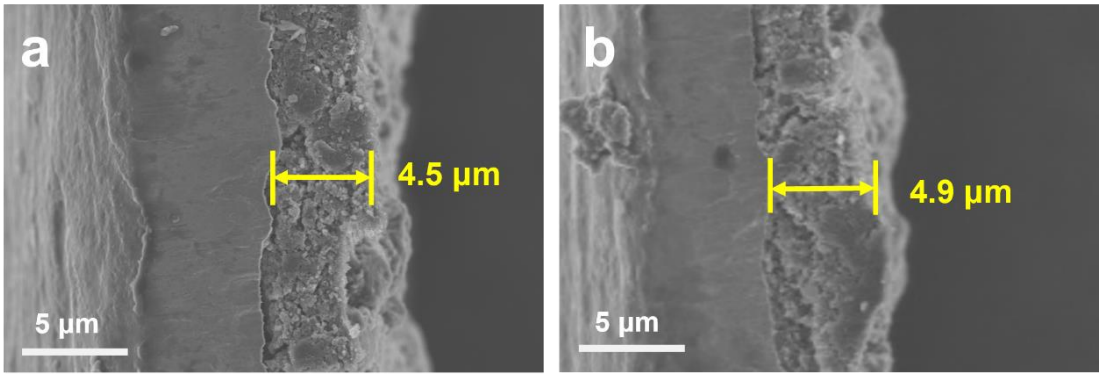

Fig. S21 Cross-sectional SEM images of the SnO_2@NPSC electrode before (a) and after (b) cycling.

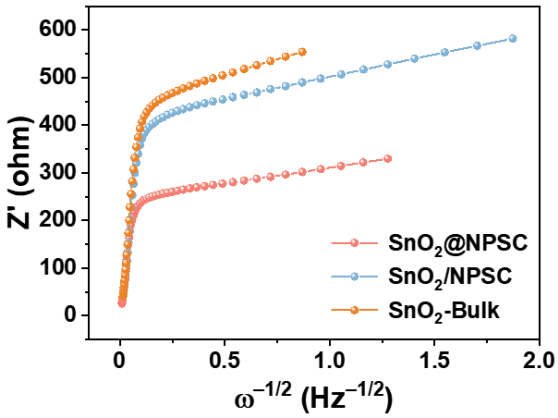

Fig. S22 The linear relationship between Z' and $\omega^{-1/2}$ in the low-frequency region for the three samples.

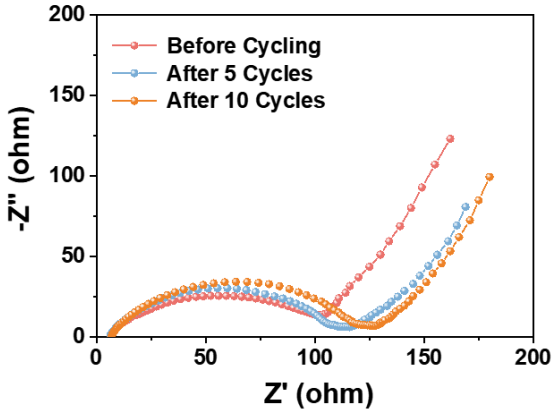

Fig. S23 Nyquist plots of the SnO_2@NPSC electrode before cycling, after 5 cycles, and after 10 cycles.

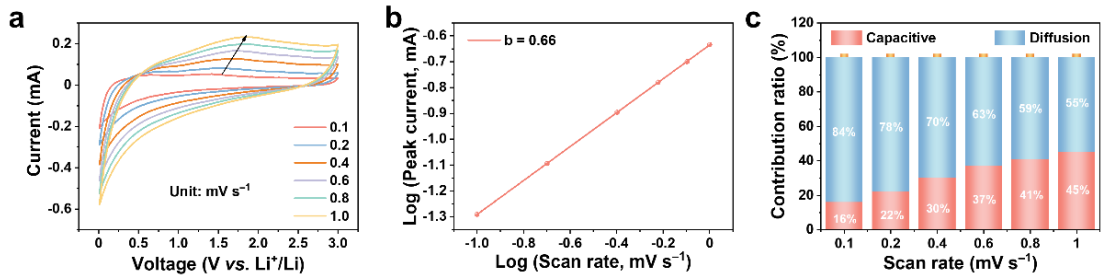

Fig. S24 CV curves at different scan rates (a), Corresponding b-values (b), Diffusion-controlled and capacitive contributions to the charge storage at various scan rates (c) of SnO_2@NPSC.

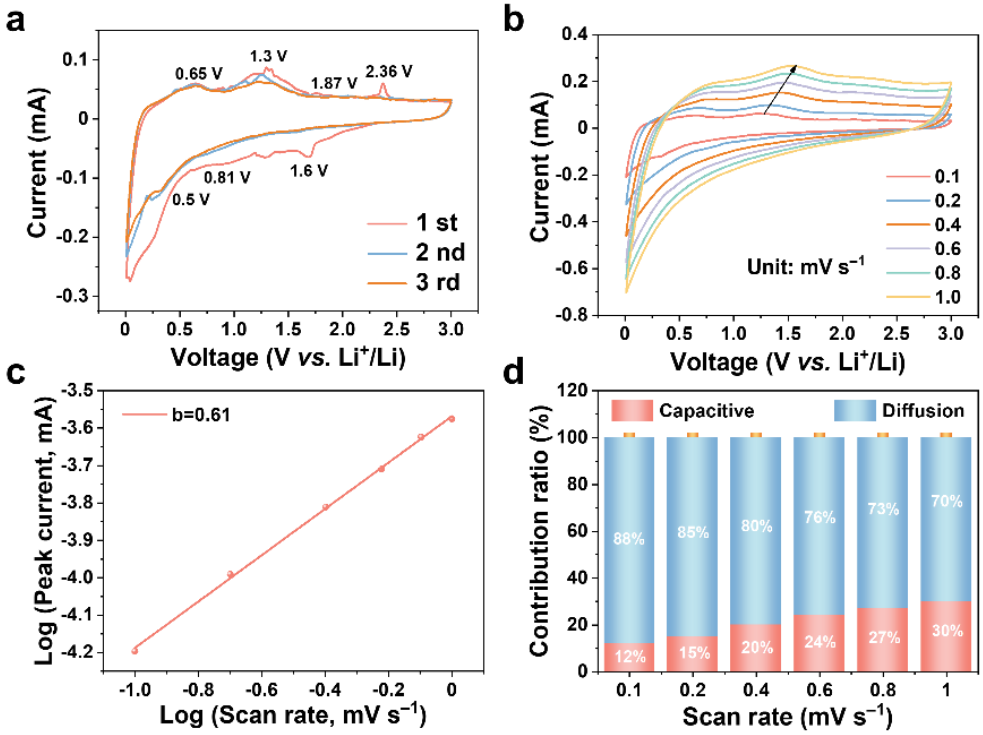

Fig. S25 CV curves for the first three revolutions at a scan rate of 0.1 mV s^{-1} (a), CV curves at different scan rates (b), Corresponding b-values (c), Diffusion-controlled and capacitive contributions to the charge storage at various scan rates (d) of SnO_2/NPSC.

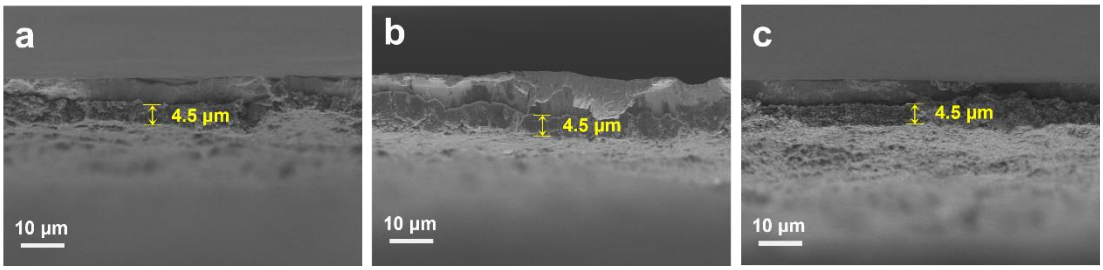

Fig. S26 Cross-sectional SEM images of SnO_2@NPSC (a), SnO_2/NPSC (b), and SnO_2-Bulk electrodes (c).

Elements	C	N	O	Sn	P	S
Relative content	49.33%	6.76%	23.83%	18.76%	0.31%	1.02%

Table S1 Relative contents of various elements derived from XPS analysis.

Electrodes	σ	D (m^2 s^{-1})
SnO_2@NPSC	68.36	$8.17*10^{-18}$
SnO_2/NPSC	91.30	$4.58*10^{-18}$
SnO_2-Bulk	130.31	$2.25*10^{-18}$

Table S2 Warburg coefficient (σ) and Li^+ diffusion coefficient (D_{Li^+}) of the three electrodes.

Equation:

$$D = \frac{R^2T^2}{2A^2n^4F^4C^2\sigma^2} \quad \text{(S1)}$$

$$i = av^b \quad \text{(S2)}$$

$$\log(i) = blog(v) + \log(a) \quad \text{(S3)}$$

$$i = k_1v + {k_2}^{1/2} \quad \text{(S4)}$$

$$i/v^{1/2} = k_1v^{1/2} + k_2 \quad \text{(S5)}$$

$$D_{Li^+} = \frac{4L^2}{\pi\tau}\left(\frac{\Delta E_S}{\Delta E_t}\right)^2 \quad \text{(S6)}$$

References

1. Z. Liang, X. Fan, H. Lei, J. Qi, Y. Li, J. Gao, M. Huo, H. Yuan, W. Zhang, H. Lin, H. Zheng and R. Cao, *Angew. Chem. Int. Ed.*, 2018, **57**, 13187-13191.

2. S. Liu, Y. Duan, X. Feng, J. Yang and S. Che, *Angew. Chem. Int. Ed.*, 2013, **52**, 6858-6862.

3. Y. Xie, *Chem. Rec.,* 2019, **19**, 2370-2384.

4. N. Issatayev, Y. Kanatbekkyzy, S. Myrzakhan, A. Mukanova, G. Kalimuldina, A. Nurpeissova and Z. Bakenov, *Energy Environ. Mater.,* 2026, **9**, e70121.